Available online at www.sciencedirect.com
ScienceDirect
Trans. Nonferrous Met. Soc. China 34(2024) 2814−2827
Transactions of Nonferrous Metals Society of China
www.tnmsc.cn

Design and characterization of biodegradable Mg−Zn−Ag metallic glasses

Jian WANG[1,2], Chen WANG[1], Wei-feng RAO[3], In-ho JUNG[2]

1. School of Mechanical Engineering, Yangzhou University, Yangzhou 225009, China;
2. Department of Materials Science and Engineering, Seoul National University, Seoul 08826, Korea;
3. School of Mechanical and Automotive Engineering, Qilu University of Technology, Jinan 250353, China

Received 7 March 2023; accepted 16 September 2023

Abstract: In order to develop the Mg−Zn−Ag metallic glasses (MGs) for biodegradable implant applications, the glass formation ability (GFA) and biocompatibility of Mg−Zn−Ag alloys were investigated using a combination of the calculation of phase diagrams (CALPHAD) and experimental measurements. High GFA potentiality of two alloy series, specifically $Mg_{96-x}Zn_xAg_4$ and $Mg_{94-x}Zn_xAg_6$ (x=17, 20, 23, 26, 29, 32, 35), was predicted theoretically and then substantiated through experimental testing. X-ray diffraction (XRD) and differential scanning calorimetry (DSC) techniques were used to evaluate the crystallinity, GFA, and crystallization characteristics of these alloys. The results showed that compositions between $Mg_{73}Zn_{23}Ag_4$ and $Mg_{64}Zn_{32}Ag_4$ for $Mg_{96-x}Zn_xAg_4$, $Mg_{66}Zn_{28}Ag_6$ and $Mg_{63}Zn_{31}Ag_6$ for $Mg_{94-x}Zn_xAg_6$ displayed a superior GFA. Notably, the GFA of the $Mg_{96-x}Zn_xAg_4$ series was better than that of the $Mg_{94-x}Zn_xAg_6$ series. Furthermore, the $Mg_{70}Zn_{26}Ag_4$, $Mg_{74}Zn_{20}Ag_6$, and $Mg_{71}Zn_{23}Ag_6$ alloys showed acceptable corrosion rates, good cytocompatibility, and positive effects on cell proliferation. These characteristics make them suitable for applications in medical settings, potentially materials as biodegradable implants.

Key words: glass forming ability; calculation phase diagram (CALPHAD); Mg−Zn−Ag metallic glasses; cytocompatibility

1 Introduction

Magnesium (Mg) alloys have been investigated as promising materials in the field of biomedicine due to their remarkable cyto-compatibility, biodegradability, high specific strength, and stiffness [1]. However, the clinical application of current commercial Mg alloys has been constrained by their high rates of corrosion and hydrogen release [2]. Fortunately, the development of Mg-based metallic glasses (MGs) provides a potential solution. By incorporating Mg with transition elements and rare earth elements, these MGs exhibit superior glass formation ability (GFA) in the supercooled liquid phase region [3]. This quality enables the potential application of Mg-based MGs as medical materials. Moreover, compared to crystalline Mg-based alloys, the Mg-based MGs exhibit superior anti-corrosion properties, mechanical strength, and hardness, as well as appropriate degradability, makes them extremely attractive for biomedical applications [4]. In terms of improved anti-corrosion and mechanical properties, Mg−Zn-based MGs, particularly Mg− Zn−Ca MGs, have made significant advancements recently.

However, the limited GFA and inherent brittleness of Mg−Zn−Ca MGs have remained challenging [5,6]. To get over these restrictions, researchers [7] have tried to add silver (Ag) and zinc (Zn) elements. The addition of Ag has been found to enhance the GFA and improve various

Corresponding author: Jian WANG, E-mail: jianwang502@snu.ac.kr
DOI: 10.1016/S1003-6326(24)66578-7
1003-6326/© 2024 The Nonferrous Metals Society of China. Published by Elsevier Ltd & Science Press
This is an open access article under the CC BY-NC-ND license (http://creativecommons.org/licenses/by-nc-nd/4.0/)

mechanical properties, including microhardness, final fracture strength, and plastic strain [8−10]. It has reported that Ag can also enhance the anti-corrosion characteristics of alloys [11,12]. Moreover, Ag has also been noted for its ability to promote bone formation and growth [13], to exhibit antibacterial characteristics [14,15], and to serve as an effective antibacterial agent [16]. Aside from that, the micro-alloying Zn into Mg-based MGs has produced promising outcomes, including enhanced corrosion resistance, mechanical capabilities, biocompatibility traits, etc. Therefore, the characteristics of Mg−Zn−Ag MGs, including desirable mechanical properties, excellent GFA, and cytocompatibility, provide a practical and effective approach to enhancing the potential of Mg-based alloys for biomedical applications.

The formation of MGs can be facilitated by avoiding the formation of crystalline phases during the rapid solidification of liquid metals. Thus, it is possible to predict compositions with optimal GFA by identifying alloy compositions with the lowest tendency to form crystalline phases [17]. The CALPHAD method is commonly employed to gather and evaluate phase equilibrium and thermodynamic properties of alloys. Through the selection of appropriate thermodynamic models, and optimization of model parameters using experimental data, a reasonable description of the Gibbs energy for each phase in the alloys system can be obtained [18]. The CALPHAD approach may be used to calculate thermodynamic characteristics related to the formability of compounds, such as driving force (DF), metastable phase equilibria, and T_0 curve, making them useful for forecasting the initial GFA of alloys [19]. In conclusion, it is feasible and efficient to develop Mg−Zn−Ag MGs as biodegradable materials combined with the CALPHAD technique.

Therefore, in this study, the phase equilibria and thermodynamic properties of the Mg−Zn−Ag ternary system were systematically evaluated and optimized using the CALPHAD method [20], which provides a solid foundation for the present and subsequent research. It also represents a novel and innovative aspect of this study. Based on these present calculations, two series of Mg−Zn−Ag alloys were created using the spinning melting process. The resulting Mg−Zn−Ag MGs were subjected to the comprehensive characterization, including the evaluations of their anti-corrosion properties and cytocompatibility through the SBF solution immersion and cell culture experiments. The ultimate goal of this work is to develop Mg−Zn−Ag-based MGs with superior GFA, desirable anti-corrosion properties, and excellent cytocompatibility, which could be considered as potential clinical applications [21−27].

2 Experimental

2.1 MGs preparation and analysis

Mg blocks with a purity of 99.8%, Ag grains with a purity of 99.9%, and Zn ingots with a purity of 99.99% were used as raw materials for preparation of $Mg_{96-x}Zn_xAg_4$ and $Mg_{94-x}Zn_xAg_6$ (x=17, 20, 23, 26, 29, 32, 35) alloys. Cubic crucibles made from Ta foil (0.15 mm in thickness) with a purity of 99.5% were utilized for the sample melting process. These alloys were melted using the induction melting method. Prior to melting, the oxidation layer on the pure metal surface was removed with diluted hydrochloric acid (~0.1% HCl). Since Zn has a low boiling point (~907 °C), the initial melting process involves the Ag and Mg elements, which were melted first to form eutectic alloys with a lower melting temperature (~600 °C). To achieve a homogeneous microstructure, all the alloys were re-melted at least three times under an argon atmosphere. The mass loss that occurred from the evaporation during the melting process was compensated for during the sample weighing process. An estimate of the evaporation mass of Mg and Zn was used to control the mass loss less than 5% for each sample. The composition of each melted sample was examined using an inductively coupled plasma emission spectrometer (ICP). The results of the analysis are presented in Table 1.

The preparation of the MGs samples was carried out using a VTC−500W furnace manufactured by Shenyang Kejing Automation Equipment Co., Ltd. The cast samples were first cut into small pieces. Then, they were placed inside a 12 mm-diameter quartz pipe with a 1 mm-diameter hole at the bottom, and positioned about 2 mm from the copper roller. The chamber was evacuated using a mechanical pump and a molecular pump to create a vacuum, and argon gas was introduced to achieve a pressure of −0.04 MPa in the vacuum chamber. The amorphous strip furnace had a copper diameter

Table 1 Characteristic temperatures of $Mg_{96-x}Zn_xAg_4$ and $Mg_{94-y}Zn_yAg_6$ (x=y=17, 20, 23, 26, 29, 32) metallic glasses obtained by DSC measurements

Sample	T_g/K	T_g^p/K	T_x/K	T_{p1}/K	T_{p2}/K	T_M/K	T_L/K
$Mg_{79}Zn_{17}Ag_4$	344.4	348.5	353.1	356.7	373.5	652.3	698.1
$Mg_{76}Zn_{20}Ag_4$	338.1	339.8	347.7	359.4	378.3	641.6	681.5
$Mg_{73}Zn_{23}Ag_4$	337.2	346.9	357.1	368.3	385.9	638.5	664.9
$Mg_{70}Zn_{26}Ag_4$	336.8	358.6	365.0	377.7	396.7	638.0	662.6
$Mg_{67}Zn_{29}Ag_4$	343.3	359.9	366.3	388.8	403.8	637.2	654.7
$Mg_{64}Zn_{32}Ag_4$	336.8	355.8	369.5	390.5	406.2	643.1	691.9
$Mg_{77}Zn_{17}Ag_6$	333.2	338.2	342.1	359.2	385.4	657.1	683.2
$Mg_{74}Zn_{207}Ag_6$	335.4	347.6	345.7	362.8	389.1	651.3	680.5
$Mg_{71}Zn_{23}Ag_6$	338.4	353.3	351.5	376.7	396.8	648.1	675.6
$Mg_{68}Zn_{26}Ag_6$	341.2	352.5	364.3	385.5	405.1	650.2	677.9
$Mg_{65}Zn_{29}Ag_6$	346.8	359.3	373.7	393.4	414.8	653.5	673.3
$Mg_{62}Zn_{32}Ag_6$	340.4	351.2	354.4	395.7	416.8	653.2	710.1

T_g: glass transition temperature; T_g^p: glass transformation peak temperature; T_x: crystallization temperature; T_p: crystallization peak temperature; T_M: melting temperature; T_L: solidification temperature

of 30 mm, and the speed was set at 1800 r/min for induction melting. Once the sample was completely melted into the liquid, the spray casting process was initiated under a pressure of −0.02 MPa, according to the vacuum meter. The final obtained ribbons had an average thickness of approximately 30 μm and a width of 2−3 mm.

The prepared samples underwent analysis using powder XRD to determine their crystallinity. The characteristic “steamed bread peak” of metallic glasses’ diffraction patterns was used to identify the MGs. XRD tests were conducted using a D8 Advance polycrystalline X-ray diffraction instrument produced by the Bruker company in Germany. In order to minimize oxidation, the samples were pre-ground into powder and liquid paraffin was added during the grinding process. The scanning range for all samples was set at 20°−90° with a scanning speed of 5 (°)/min. XRD profiles were acquired using 45 kV and 40 mA Cu K_α irradiation.

2.2 Biocompatibility and biodegradability analysis

2.2.1 SBF solution immersion test

The immersion test was conducted to evaluate the anti-corrosion properties of MGs samples. The pH of the SBF solution was adjusted to 7.4 using NaOH and $NaHCO_3$. The mass of each sample was measured using an electronic balance. The SBF solution composition consisted of 8.035 g/L NaCl, 0.355 g/L $NaHCO_3$, 0.225 g/L KCl, 0.231 g/L $K_2HPO_4·3H_2O$, 0.311 g/L $MgCl_2·6H_2O$, 0.292 g/L $CaCl_2$, 0.072 g/L $MgSO_4$, 0.06 g/L $NaHPO_4$, 1 m/L HCl, and pure water. Ribbons with an average size of 30 m in thickness, 2−3 mm in breadth, and 10 mm in length were used for the present immersion test.

The prepared MG samples were placed in the SBF solution and incubated at 37 °C with 5% CO_2 for 3 d. The ratio of MGs sample surface area to the volume of the SBF solution is 1.25 cm^2/mL. The SBF solution was renewed every 24 h. The samples were taken out, then rinsed with deionized water and dried after the 1, 2, and 3 d immersion. After that, corrosion products were removed from the samples using a solution of 100 g of NH_4C1 and 1000 mL of deionized water. Subsequently, the samples were reweighed using an electronic balance. The average corrosion rate (CR, mm/a) can be calculated using the following equation:

$$CR=\frac{Km}{ATρ} \tag{1}$$

where the constant K is 8.76×10^4; m is the mass loss; A is the contact area; T is the soaking time; ρ is the density.

2.2.2 Cytotoxicity evaluation

Murine fibroblast cells (L929) were used in the

in vitro cell culture experiment. The L929 cells were cultured in Dulbecco's modified Eagle's medium (DMEM, Invitrogen Gibco) supplemented with 10% fetal bovine serum (FBS, Hyclone) and penicillin/streptomycin (100 U/mL each). The cells were cultured in a humid incubator set to be 37 °C, with 95% relative humidity and 5% CO_2. 2.4×10^5 cells in 1 mL of cell culture media were seeded into 24-well plates for the experiment, resulting in a surface area to medium ratio of 1.25 cm^2/mL. The L929 cells were cultured directly on the surfaces of the samples for 1, 4, and 7 d, respectively. A control group was set up with only blank medium containing the same concentration of L929 cells. The morphology of cultured L929 cells was observed using a high-magnification light microscope (BDS 400), and various assay procedures were performed at each selected time point.

2.2.3 Cell proliferation evaluation

The L929 cells soaked for 7 d were further assessed for the cytotoxicity evaluation to investigate the effect of the two series of Mg−Zn−Ag MGs on the cell proliferation culture. The L929 cells were stained with DAPI (Invitrogen, US) to visualize the total nuclei, which appears blue. Additionally, EDU (E6032, US EVERBRIGHT INC, China) staining was performed to identify new nuclei, which are labeled as green. This staining technique allows for the assessment of cell proliferation in response to the Mg−Zn−Ag MGs.

3 Results and discussion

3.1 Composition design of Mg−Zn−Ag MGs with CALPHAD method

3.1.1 Thermodynamic modeling of Mg−Zn−Ag ternary system

The phase equilibria of the Mg−Zn−Ag ternary system were modeled using the FactSage software [28]. Thermodynamic parameters from previous studies on the Mg−Zn [29], Mg−Ag [30], and Ag−Zn [31] binary systems were employed with slight modification. The solid phases were modeled using the compound energy formalism model [32] with sublattice structures, such as $(Ag,Mg,Zn)_m(Ag,Mg,Zn)_n$. The final calculated phase diagrams of the Mg−Zn, Mg−Ag, and Zn−Ag binary subsystems are presented in Fig. 1.

The ternary thermodynamic parameters of the liquid phase (in the Mg-rich region) were optimized

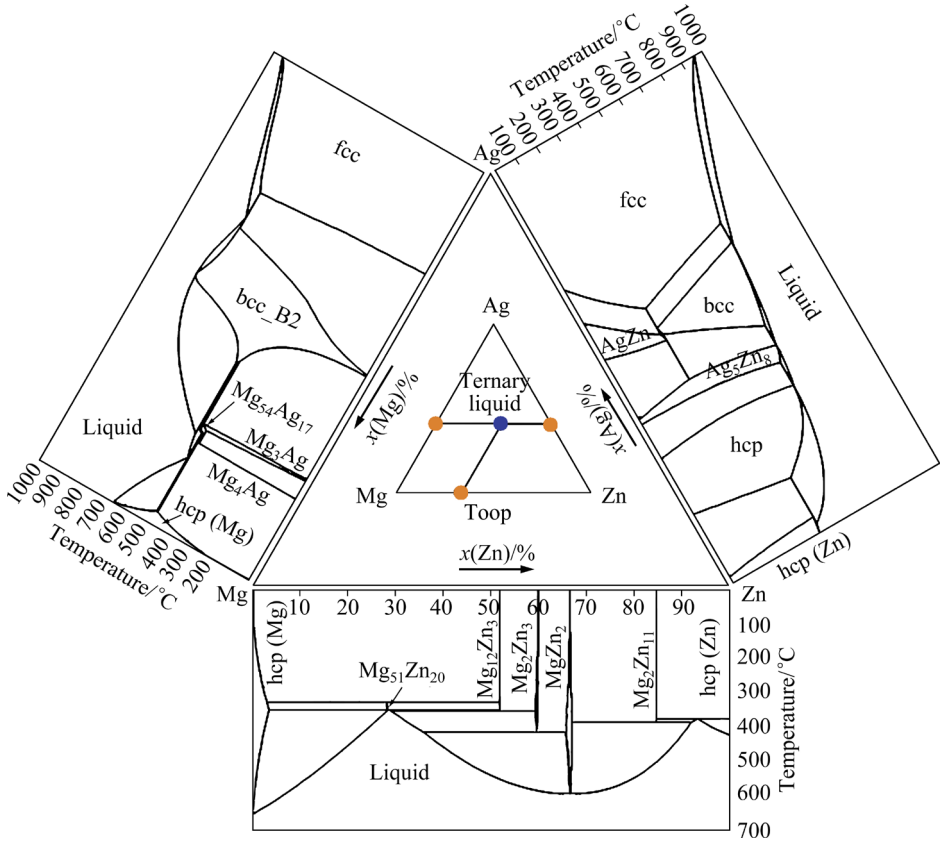

Fig. 1 Calculated phase diagrams of binary sub-systems of Mg−Zn−Ag ternary system

based on the DSC results obtained in this study. The Gibbs energy of the ternary liquid phase was derived from the three binary subsystems using the 'Troop-like' interpolation technique [33] (see Fig. 1). The melting temperatures of $Mg_{96-x}Zn_xAg_4$ and $Mg_{94-x}Zn_xAg_6$ (x=17, 20, 23, 26, 29, 32, 35) alloys were measured using DSC (as summarized in Table 1). The ternary parameters of the liquid phase were optimized accordingly. The present calculated isothermal section of the Mg−Zn−Ag ternary system at 300 °C, along with experimental data [34], is present in Fig. 2. The isopleths of MgZn−4Ag and MgZn−6Ag, calculated using the present obtained thermodynamic parameters, are in good agreement with the DSC results (see Fig. 3). The present modeling work successfully reproduced all the experimental results, as illustrated in Figs. 2 and 3.

3.1.2 Theoretical calculation of GFA in Mg−Zn−Ag alloys

As mentioned above, the prediction of GFA can be achieved by calculating the DFs of all crystalline phases of alloys during the solidification

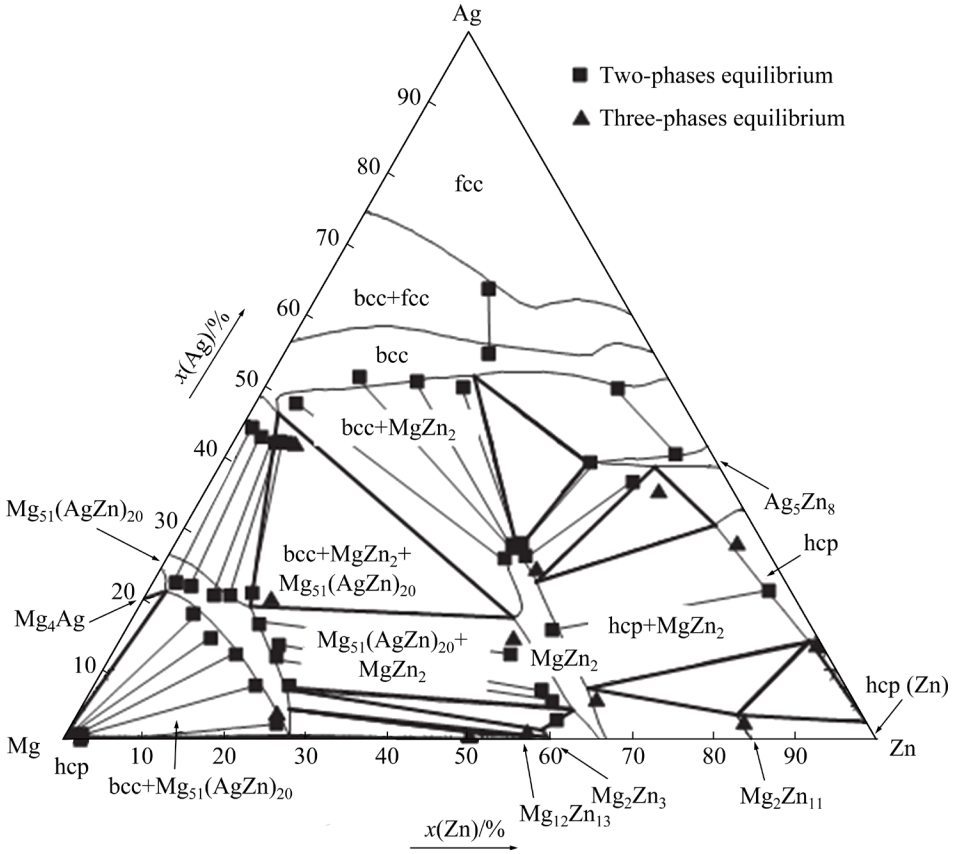

Fig. 2 Calculated isothermal section of Mg−Zn−Ag ternary system at 300 °C with experimental data [34]

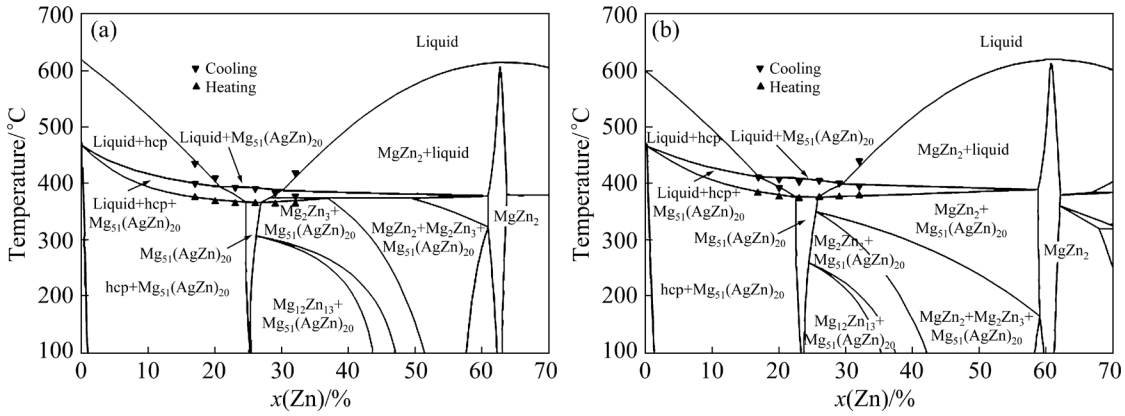

Fig. 3 Calculated isopleths of MgZn−4Ag (a) and MgZn−6Ag (b) systems with present experimental data measured using DSC technique

process. In the case of the Mg−Zn binary system, the DFs of all crystalline phases at 300 °C were calculated using the self-consistent thermodynamic database developed in this study (see Fig. 4(a)). The DFs of crystalline phases were plotted as a function of decreasing Mg content, exhibiting a "U" shaped curve with a minimum point at approximately 72 at.% Mg, as shown in Fig. 4(a). According to this criterion, the optimal composition range for achieving amorphous formation in Mg−Zn alloys is expected to fall within this composition region, where the DFs are minimized. It is noted that the present calculations have a good agreement with previous experimental data [33,34], which demonstrated that the metallic glass formation region was identified at 20−35 at.% Zn in the Mg−Zn binary system.

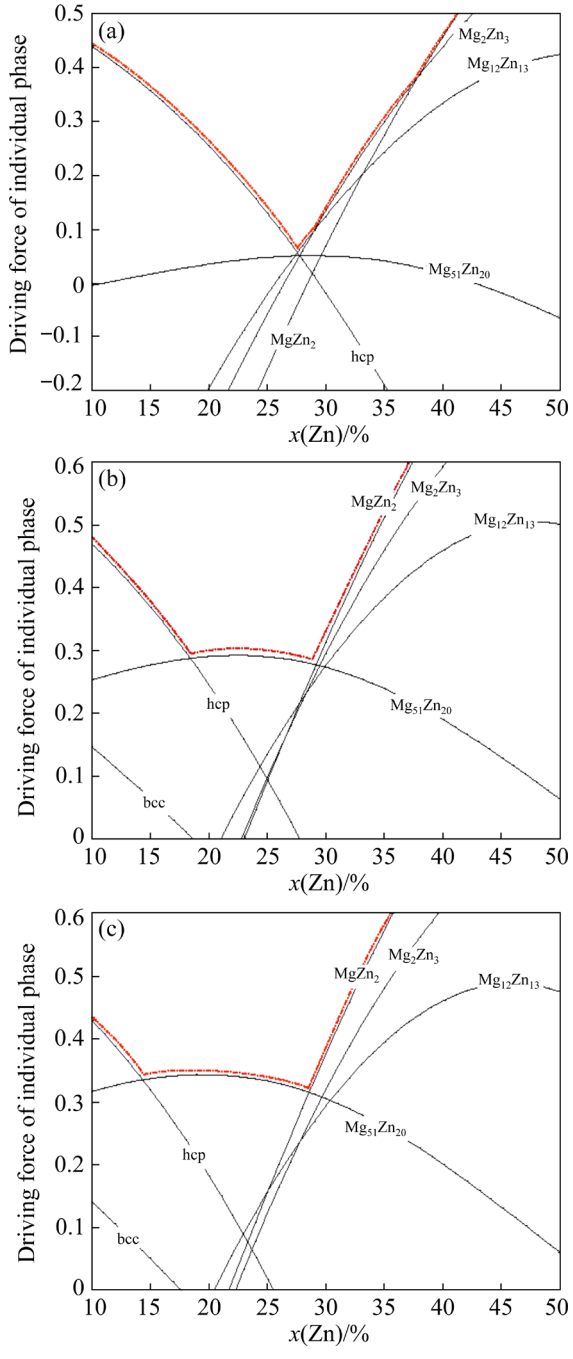

Fig. 4 Calculated DFs for individual crystalline phases and composition range of glass formation for Mg−Zn (a), $Mg_{96-x}Zn_xAg_4$ (b), and $Mg_{94-x}Zn_xAg_6$ (c) alloys

Upon comparison with the results obtained for Mg−Zn system (see Fig. 4(a)), it can be concluded that Mg−Zn−Ag alloys also exhibit a favorable composition range with better GFA, which can be predicted using the CALPHAD methodology. To verify this, two series compositions of alloys, $Mg_{96-x}Zn_xAg_4$ and $Mg_{94-x}Zn_xAg_6$, were selected. The DFs of crystalline phases were calculated for both series at 300 °C, as shown in Figs. 4(b, c). The curves of the DFs obtained for both series also demonstrated a "U" shape, with the lowest DFs value in the composition range of 19 at.% to 29 at.% Zn for Mg_{96-x}ZnxAg$_4$ alloys and 15 at.% to 28 at.% Zn for $Mg_{94-x}Zn_xAg_6$ alloys, respectively. Furthermore, as shown in Figs. 4(b, c), the composition range with the lowest DF shifts towards the Mg-rich region with an increasing Ag component. In other words, alloys with 4 at.% Ag are expected to exhibit better GFA compared with those with 6 at.% Ag, as indicated by their relatively low DF. Additionally, the calculation results suggest that the addition of Ag leads to a smoother change in the GFA of the Mg−Zn alloy compared with the binary Mg−Zn alloys, as illustrated in Fig. 4. Moreover, for a fixed Ag composition, the variation trend of GFA in Mg−Zn−Ag alloys closely aligns with that of the Mg−Zn binary alloys. However, the alloy composition with the highest GFA shifts from $Mg_{73}Zn_{27}$ to $Mg_{67}Zn_{29}Ag_4$ and $Mg_{65}Zn_{29}Ag_6$.

3.2 Effect of Zn and Ag components on crystallization and thermal stability of Mg−Zn−Ag MGs

The thermodynamic database was utilized to calculate the Mg−Zn−Ag system, which led to the experimental preparation of 14 samples with nominal compositions varying of 4 at.% Ag as $Mg_{96-x}Zn_xAg_4$ and 6 at.% Ag as $Mg_{94-x}Zn_xAg_6$ (x=17, 20, 23, 26, 29, 32, 35). The XRD analysis was performed on the free side of the as-prepared Mg−Zn−Ag strip samples. The present obtained XRD patterns are illustrated in Fig. 5. The XRD

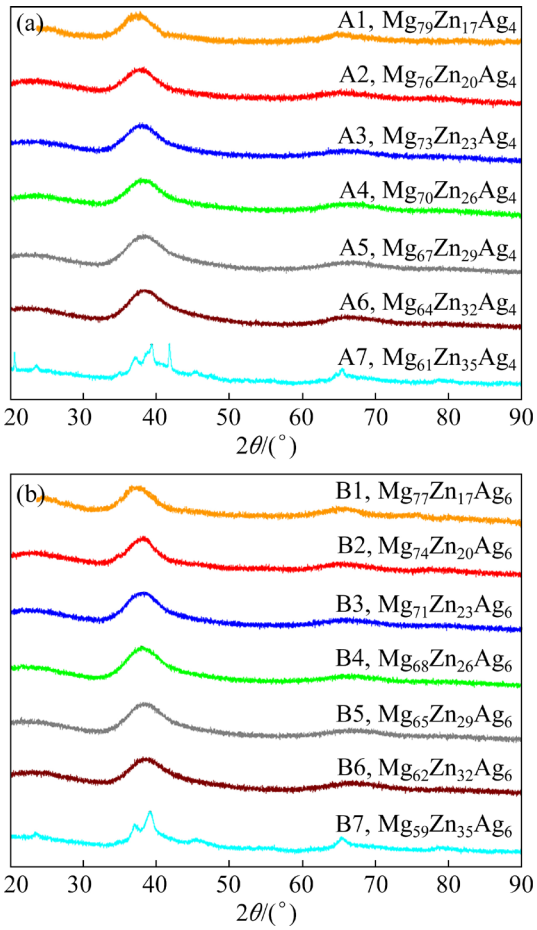

Fig. 5 XRD patterns obtained from free side of Mg−Zn−Ag MGs: (a) $Mg_{96-x}Zn_xAg_4$; (b) $Mg_{94-x}Zn_xAg_6$

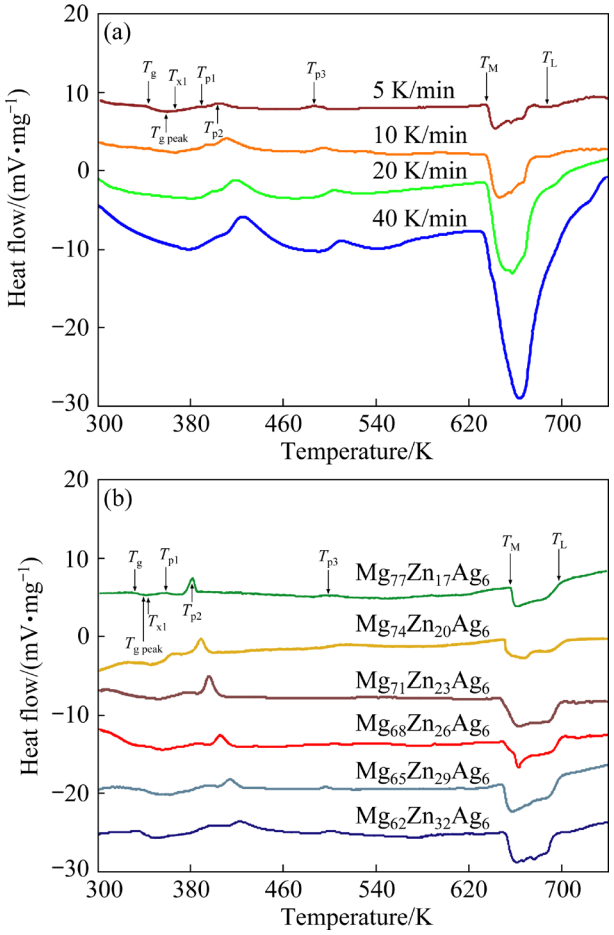

Fig. 6 DSC curves of Mg−Zn−Ag MGs showing metallic glasses formation, crystallization and melting behavior: (a) $Mg_{67}Zn_{29}Ag_4$ with heating rates of 5, 10, 20 and 40 K/min; (b) $Mg_{94-x}Zn_xAg_6$ with heating rate of 5 K/min

data confirmed that all samples, except for A7 ($Mg_{61}Zn_{35}Ag_4$) and B7 ($Mg_{59}Zn_{35}Ag_6$), exhibited broad diffraction peaks spanning 2θ of 38°−66° without any crystalline diffraction peaks, indicating their non-crystalline (metallic glass) nature. Additionally, the broad scattering maximum observed in Fig. 5 was slightly shifted towards a higher diffraction angle, which can be attributed to the atomic substitution of Mg atoms with the smaller atomic radius of Zn atoms, resulting in a slightly altered atomic arrangement.

Figure 6(a) illustrates the dependence of the characteristic temperature on the heating rate for the $Mg_{67}Zn_{29}Ag_4$ MG sample. It can be observed that these characteristic temperatures increase with the increasing heating rate. Figure 6(b) illustrates the characteristic temperatures of $Mg_{94-x}Zn_xAg_6$ (x=17, 20, 23, 26, 29, 32, 35) MGs using DSC with a heating rate of 5 K/min.

The composition dependence of the reduced glass transition temperature (T_{rg}=T_g/T_m) for both series of MGs is illustrated in Fig. 7(a). The calculated results indicate that the regions with superior GFA fall within the composition ranges of $Mg_{73}Zn_{23}Ag_4$ to $Mg_{64}Zn_{32}Ag_4$ for $Mg_{96-x}Zn_xAg_4$, and $Mg_{66}Zn_{28}Ag_6$ to $Mg_{63}Zn_{31}Ag_6$ for $Mg_{94-x}Zn_xAg_6$. Additionally, it is observed that $Mg_{96-x}Zn_xAg_4$ alloys exhibit better GFA compared with $Mg_{94-x}Zn_xAg_6$ alloys, which aligns with the prediction from the thermodynamic database calculations presented in Fig. 4. This finding addresses the limitation of the restricted size of existing Mg−Zn−Ca metallic glasses [6].

The apparent activation energy (AE, E) of each characteristic transformation was calculated by the Kissinger method [35]. The Kissinger equation is based on the shift of the DSC curves with respect to different heating rates and is given by

$$\ln(B/T^2)=-E/(RT)+C \quad (2)$$

where B is the heating rate, E is the activation

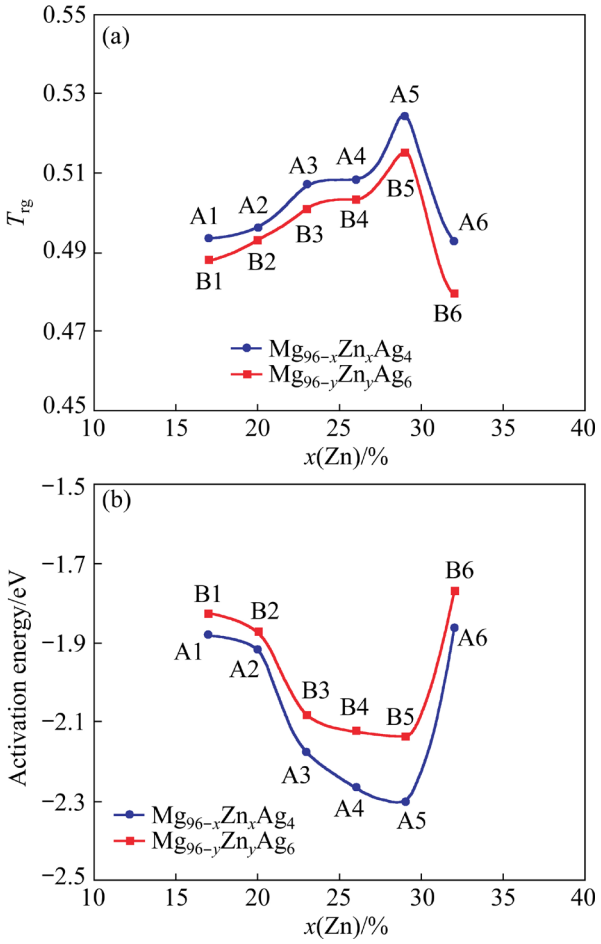

Fig. 7 Composition dependence of reduced glass transition temperature T_{rg} (a) and activation energies (b) of Mg−Zn−Ag alloys

energy, R is the gas molar constant, C is a constant, and T is the characteristic temperature (such as T_g and T_x). The calculated values of E are presented in Fig. 7(b). Alloys with more negative E values are expected to have higher anti-crystallization ability, indicating easier formation of MGs. The highest E values were observed for $Mg_{67}Zn_{29}Ag_4$ and $Mg_{65}Zn_{29}Ag_6$, suggesting that they have the highest GFA. Moreover, the $Mg_{96-x}Zn_xAg_4$ alloys exhibited a wider formation range and better GFA compared with the $Mg_{94-x}Zn_xAg_6$ alloys. These findings are consistent with those obtained from DFs calculations (Fig. 4) and T_{rg} measurements (Fig. 7(a)). The experimental findings confirm that the GFA effect of Ag addition on the Mg−Zn alloys follows a similar tendency observed in the binary Mg−Zn alloys. However, there is a shift in the composition of the ternary alloys with the highest GFA, as shown in Figs. 4 and 7.

3.3 Effect of component on biocompatibility and biodegradability of Mg−Zn−Ag MGs

3.3.1 Immersion

According to the previous studies [36,37], degradable Mg-based alloys should have corrosion rate below 0.5 mm/a in order to be appropriate for clinical applications. The corrosion rates of the $Mg_{96-x}Zn_xAg_4$ and $Mg_{94-x}Zn_xAg_6$ MGs submerged in SBF solution for 1, 2 and 3 d were therefore assessed, as shown in Fig. 8. It can be observed that the corrosion rates of the present samples are lower than those of Mg− Zn−Ca MGs (1.04±0.83 mm/a for 12 weeks) [5]. This may be due to the instability of the corrosion product layer formed on the sample surface during immersion, which does not provide long-term protection against erosion [38].

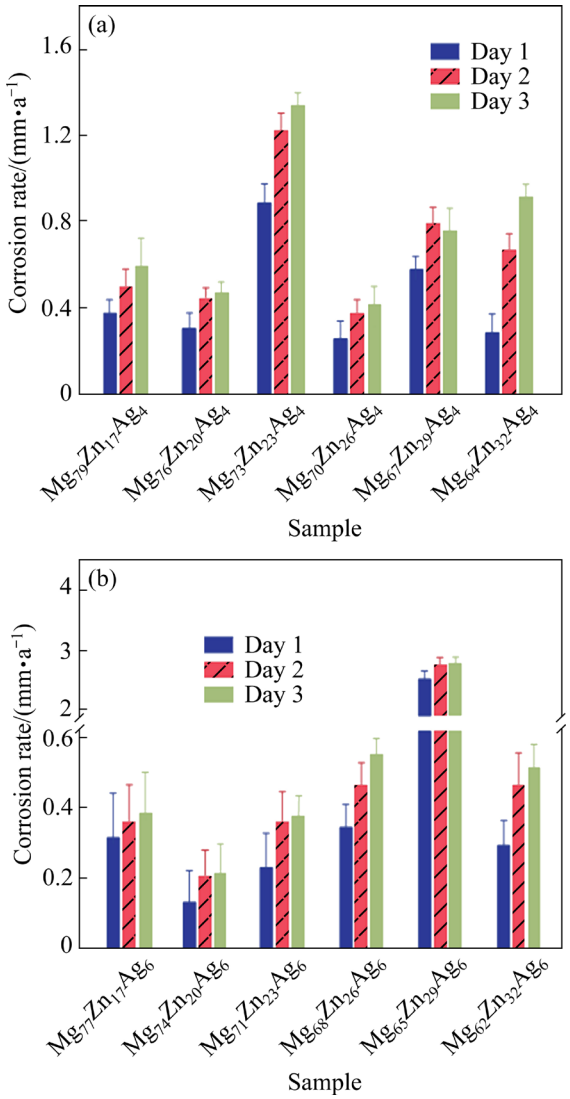

Fig. 8 Corrosion rates of $Mg_{96-x}Zn_xAg_4$ (a), and $Mg_{94-x}Zn_xAg_6$ (b) immersed in SBF solution for 1, 2 and 3 d, respectively

According to the current findings, the tendency in corrosion rates of the Mg−Zn−Ag MGs did not show a clear linear correlation with the composition change in Ag and Zn elements, indicating that the anti-corrosion ability of these alloys was also affected by additional unclear factors. Overall, the corrosion resistance of the $Mg_{94-x}Zn_xAg_6$ MGs was higher than that of the $Mg_{96-x}Zn_xAg_4$ MGs. Samples A4 and B2 had average corrosion rates of (0.25±0.08) and (0.13±0.1) mm/a following immersion, respectively. However, the corrosion rates of these samples increased significantly after 3 days of immersion, reaching (0.41±0.08) and (0.22±0.07) mm/a, respectively. In summary, Samples A2 and A4, as well as Samples B1, B2, and B3, meet the suggested corrosion rate criterion for orthopedic implantation.

3.3.2 Cytotoxicity

The cytotoxicity of the Mg−Zn−Ag MGs was assessed through cell culture experiments using L929 cells. The proportion of cell death was measured after culturing the cells directly on the alloys for 1, 4 and 7 d. The results are plotted in Fig. 9. The cell death proportion increased for all samples with increasing incubation time. This trend was similar to the corrosion rate trend observed for the alloys (see Fig. 8), which indicates a correlation between corrosion rate and cell death proportion. Fewer metal ions are released when the corrosion rate is lower, which reduces the cytotoxicity of the alloys to cells. While Samples B2 and B3 displayed comparable cell death proportions to the control group, which were below 1%. Sample A4 displayed a slightly higher cell death proportion in comparison to the control group. These findings were consistent with the immersion test results, highlighting the significant impact of anti-corrosion properties on cytotoxicity [39].

Figure 10 shows the cell morphologies of the L929 cells cultured on Samples A4, B2 and B3 as well as the control group. The L929 cells on Samples A4, B2, and B3 exhibited minimal pathological changes and retained high activity levels (Figs. 10(d, g, j)) after 1 d of culture, similar to the control group (Fig. 10(a)). The morphology of L929 cells on Samples A4, B2 and B3 remained unchanged after 4 and 7 d of culture, except for a small number of dead cells (<1%), indicating low cytotoxicity. This can be attributed to the formation of a corrosion product film on the Mg−Zn−Ag MGs, which hinders the release of Ag ions and consequently reduces the cytotoxicity of the MGs.

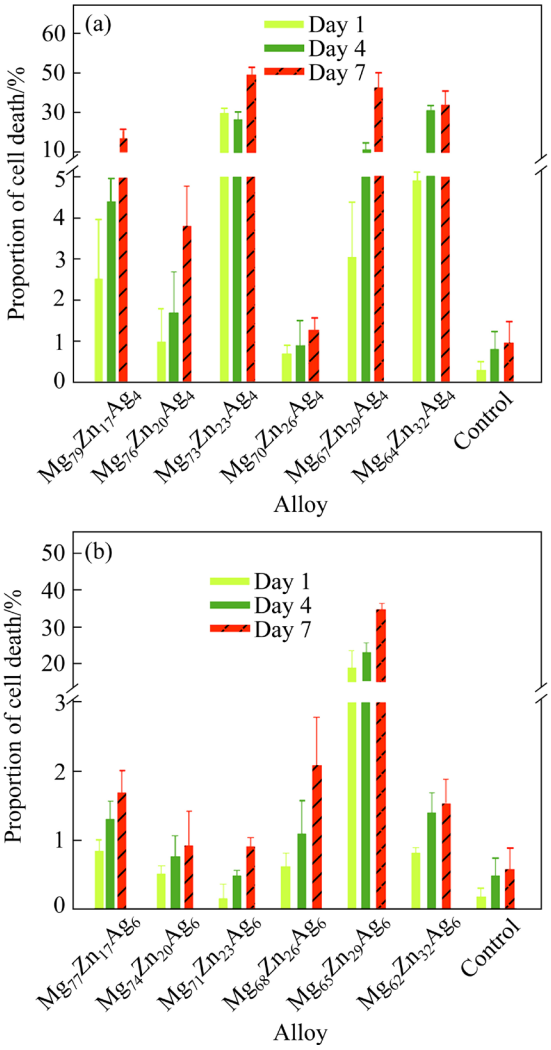

Fig. 9 Cell death proportion of control group and L929 cells cultured on Mg−Zn−Ag amorphous alloys for 1, 4, and 7 d: (a) $Mg_{96-x}Zn_xAg_4$; (b) $Mg_{94-x}Zn_xAg_6$

3.3.3 Cell proliferation

A high-content image analysis performed to quantitatively assess the impact of the two series of Mg−Zn−Ag MGs on the proliferation of L929 cells is shown in Fig. 11. The results indicate that the L929 cells are able to proliferate normally on both types of Mg−Zn−Ag MGs.

Additionally, the biocompatibility of Mg−Zn−Ag MGs was confirmed by observing the normal proliferation of L929 cells cultured on these materials. Among the two series of MGs analyzed,

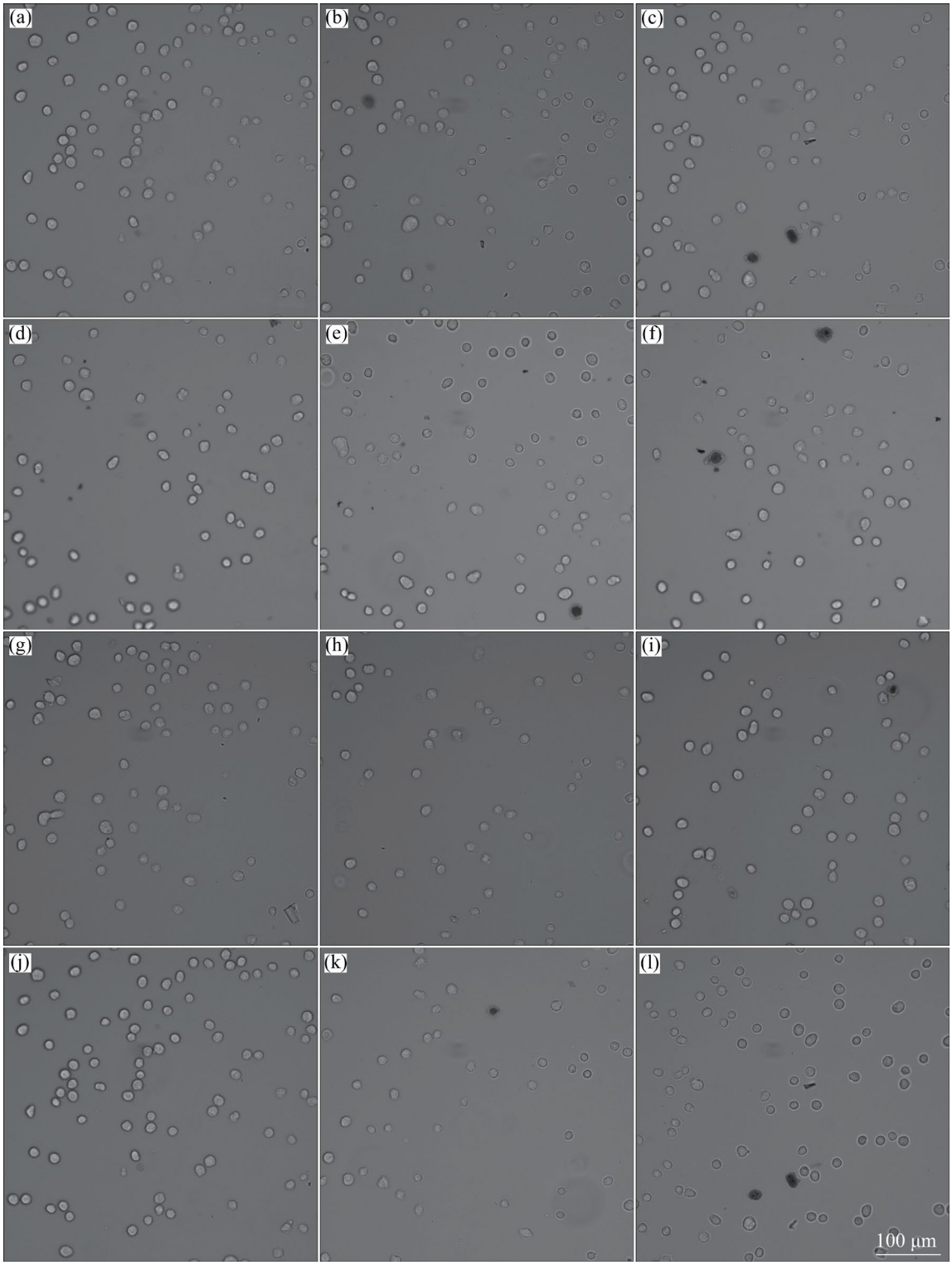

Fig. 10 Cell morphologies of control group and L929 cells cultured on Mg−Zn−Ag MGs for different time: (a) Control group, 1 d; (b) Control group, 4 d; (c) Control group, 7 d; (d) $Mg_{70}Zn_{26}Ag_4$, 1 d; (e) $Mg_{70}Zn_{26}Ag_4$, 4 d; (f) $Mg_{70}Zn_{26}Ag_4$, 7 d; (g) $Mg_{74}Zn_{20}Ag_6$, 1 d; (h) $Mg_{74}Zn_{20}Ag_6$, 4 d; (i) $Mg_{74}Zn_{20}Ag_6$, 7 d; (j) $Mg_{71}Zn_{23}Ag_6$, 1 d; (k) $Mg_{71}Zn_{23}Ag_6$, 4 d; (l) $Mg_{71}Zn_{23}Ag_6$, 7 d

$Mg_{96-x}Zn_xAg_4$ showed only slight difference in the cell division ability of L929 cells, while $Mg_{94-x}Zn_xAg_6$ showed more significant variation among Samples B1 to B6. Sample B4 showed the best capacity for cell division, whereas Sample B5 had the worst capacity. L929 cells, in particular,

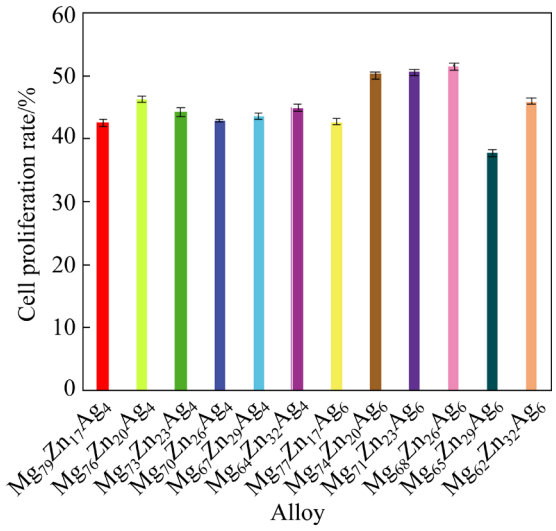

Fig. 11 Cell proliferation of L929 cells cultured on Mg−Zn−Ag amorphous alloys for 7 d

showed enhanced cell proliferation rates greater than 50% in Samples B2, B3 and B4.

Additionally, before and after cell divisions, representative images of L929 cell nuclei on Samples B2, B3 and B4 are shown in Fig. 12. The total nuclei of L929 cells cultivated on Samples B3, B4 and B5 can be obtained in Figs. 12(a−c). Similarly, in Figs. 12(d−f), the green-stained new nuclei of L929 cells on Samples B3, B4 and B5 are visualized to demonstrate cell proliferation more effectively. It is worth noting that the number of new nuclei of L929 cells cultured on Samples B3 and B4 is higher compared with that on Sample B5. The evident proliferative behavior of L929 cells on B3, B4 and B5 strongly suggests that Mg−Zn−Ag MGs can effectively promote the cell proliferation, confirming their excellent cytocompatibility.

4 Conclusions

(1) Using the CALPHAD technique, the GFA of Mg−Zn−Ag alloys was evaluated. Based on the predictions, $Mg_{96-x}Zn_xAg_4$ and $Mg_{94-x}Zn_xAg_6$ (x=17, 20, 23, 26, 29, 32, 35) alloys were designed and prepared. XRD analysis confirmed that the samples of $Mg_{96-x}Zn_xAg_4$ and $Mg_{94-x}Zn_xAg_6$ alloys (x=17, 20, 23, 26, 29, 32) were completely amorphous. DSC analysis revealed that the composition regions of $Mg_{73}Zn_{23}Ag_4$ to $Mg_{64}Zn_{32}Ag_4$ and $Mg_{66}Zn_{28}Ag_6$ to $Mg_{63}Zn_{31}Ag_6$ exhibited superior GFA for $Mg_{96-x}Zn_xAg_4$ and $Mg_{94-x}Zn_xAg_6$, respectively. Moreover, the $Mg_{96-x}Zn_xAg_4$ alloys demonstrated a wider formation range and higher GFA compared with the $Mg_{94-x}Zn_xAg_6$ alloys.

(2) In terms of corrosion resistance property, the $Mg_{94-x}Zn_xAg_6$ amorphous alloys showed superior anti-corrosion properties compared with the $Mg_{96-x}Zn_xAg_4$ alloys. Notably, the corrosion rates of Samples A2, A4, B1, B2 and B3 were within the recommended range medical application.

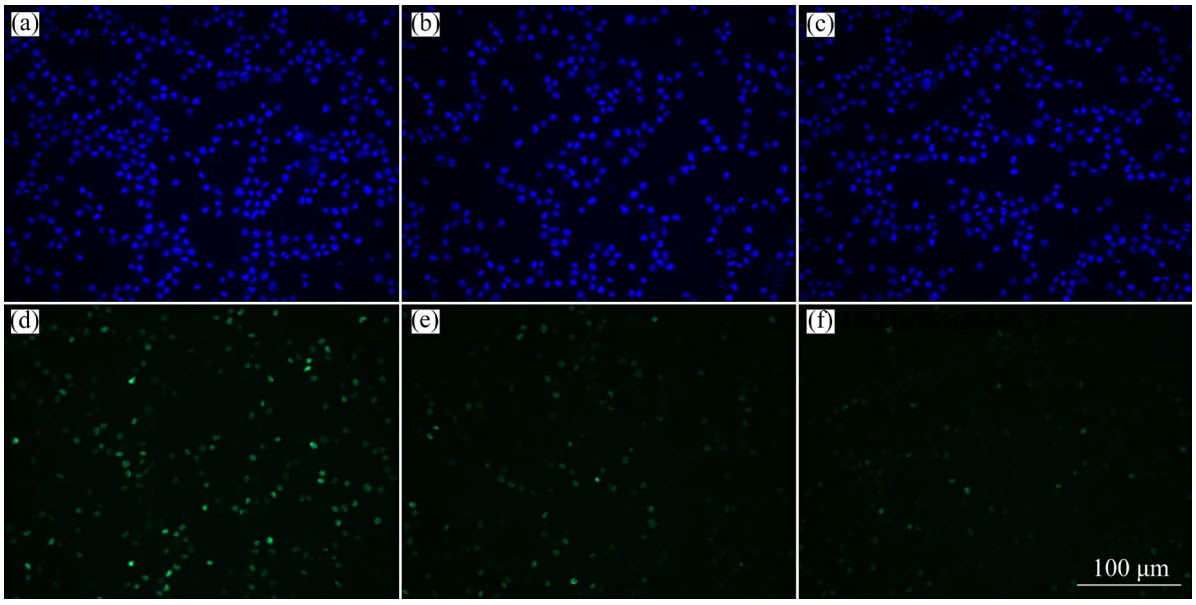

Fig. 12 Images of cell proliferation showing total nuclei (in blue) and newly formed nuclei (in green) of L929 cells cultured for 7 d on $Mg_{71}Zn_{23}Ag_6$ (a, b) and $Mg_{65}Zn_{29}Ag_6$: $Mg_{68}Zn_{26}Ag_6$ (c, d), and B5-$Mg_{65}Zn_{29}Ag_6$ (e, f)

Additionally, the present findings indicated that Mg−Zn−Ag amorphous alloys had a positive effect on the cell proliferation.

(3) Based on the present results, it can be concluded that Mg−Zn−Ag metallic glasses exhibit favorable degradability and excellent cellular compatibility, making them a promising choice for implantable biomaterials. These findings contribute to our objective of developing multi-component Mg-based alloys for biodegradable implants.

CRediT authorship contribution statement

Jian WANG: Writing − Reviewing and editing; Supervision; **Chen WANG:** Experiments and modeling, Writing − Original draft preparation; **Wei-feng RAO:** Modeling; Writing − Reviewing; **In-ho JUNG:** Supervision; Validation.

Declaration of competing interest

The authors declare that they have no known competing financial interests or personal relationships that could have appeared to influence the work reported in this paper.

Acknowledgments

The authors are grateful to the financial supports from the Shenzhen Basic Research Project, China (No. JCYJ20170815153210359), and the National Natural Science Foundation of China (No.12174210).

References

[1] TIAN Yuan, MIAO Hong-wei, NIU Jia-lin, HUANG Hua, KANG Bin, ZENG Hui, DING Wen-jiang, YUAN Guang-yin. Effects of annealing on mechanical properties and degradation behavior of biodegradable JDBM magnesium alloy wires [J]. Transactions of Nonferrous Metals Society of China, 2021, 31(9): 2615−2625.

[2] MA Ying-zhong, WANG De-xing, LI Hong-xiang, YANG Chang-ling, YUAN Fu-song, ZHANG Ji-shan. Microstructure, mechanical properties and corrosion behavior of quaternary Mg−1Zn−0.2Ca−*x*Ag alloy wires applied as degradable anastomotic nails [J]. Transactions of Nonferrous Metals Society of China, 2021, 31: 111−124.

[3] DAMBATTA M S, IZMAN S, YAHAYA B, LIM J Y, KURNIAWAN D. Mg-based bulk metallic glasses for biodegradable implant materials: A review on glass forming ability, mechanical properties, and biocompatibility [J]. Journal of Non-Crystalline Solids, 2015, 426: 110−115.

[4] NIE J F, MUDDLE B C. Precipitation hardening of Mg−Ca(−Zn) alloys [J]. Scripta Materialia, 1997, 37(10): 1475−1481.

[5] CHO S Y, CHAE S W, CHOI K W, SEOK H K, KIM Y C, JUNG J Y,YANG S J, KWON G J, KIM J T, ASSAD M. Biocompatibility and strength retention of biodegradable Mg−Ca−Zn alloy bone implants [J]. Journal of Biomedical Materials Research (Part B): Applied Biomaterials, 2013, 101(2): 201−212.

[6] JIN Chao, LIU Zhi-yuan, YU Wei, QIN Chunling, YU Hui, WANG Zhi-feng. Biodegradable Mg−Zn−Ca based metallic glasses [J]. Materials, 2022, 15(6): 2172.

[7] SUNG D S, KWON O J, FLEURY E, KIM K B, LEE J C, KIM D H, KIM Y C. Enhancement of the glass forming ability of Cu−Zr−Al alloys by Ag addition [J]. Metals and Materials International, 2004, 10: 575−579.

[8] MA Han, SHI Ling-Ling, XU Jian, LI Yi, MA En. Improving glass-forming ability of Mg−Cu−Y via substitutional alloying: Effects of Ag versus Ni [J]. Journal of Materials Research, 2006, 21(9): 2204−2214.

[9] PARK E S, KANG H G, KIM W T, KIM D H. The effect of Ag on the glass forming ability and crystallization in Mg−Cu−Ag−Y alloys [J]. Materials Science Forum, 2001, 360/361/362: 95−100.

[10] WANG Jian, MENG Ling-zhong, ZHANG Zhang, SA Bai-sheng, FU Xiao-xiao, SHENG Li-yuan, XU Dao-kui, ZHENG Yu-feng. Investigation on the crystal structure and mechanical properties of the ternary compound $Mg_{11-x}Zn_xSr$ combined with experimental measurements and first-principles calculations [J]. Journal of Magnesium and Alloys, 2023, 11(3): 1074−1082.

[11] WANG Li-qing, QIN Gao-wu, SUN Shi-neng, REN Yu-ping, LI Song. Effect of solid solution treatment on in vitro degradation rate of as-extruded Mg−Zn−Ag alloys [J]. Transactions of Nonferrous Metals Society of China, 2017, 27(12): 2607−2612.

[12] ZHAO Hong, WANG Li-qing, REN Yu-ping, YANG Bo, LI Song, QIN Gao-Wu. Microstructure, mechanical properties and corrosion behavior of extruded Mg–Zn–Ag alloys with single-phase structure [J]. Acta Metallurgica Sinica (English Letters), 2018, 31(6): 575−583.

[13] JÄHN K, SAITO H, TAIPALEENMÄKI H, GASSER A, HORT N, FEYERABEND F, SCHLÜTER H, RUEGER J M, LEHMANN W, WILLUMEIT-RÖMER R, HESSE E. Intramedullary Mg_2Ag nails augment callus formation during fracture healing in mice [J]. Acta Biomaterialia, 2016, 36: 350−360.

[14] LI Xiao-yun, GAO Guan-hui, SUN Cheng-jun, ZHU Yao-yao, QU Ling-yun, JIANG Feng-hua, DING Hai-bing. Preparation and antibacterial performance testing of Ag nanoparticles embedded biological materials [J]. Applied Surface Science, 2015, 330: 237−244.

[15] GUDIKANDULA K, MARINGANTI S C. Synthesis of silver nanoparticles by chemical and biological methods and their antimicrobial properties [J]. Journal of Experimental Nanoscience, 2016, 11(9): 714−721.

[16] MELAIYE A, YOUNGS W J. Silver and its application as an antimicrobial agent [J]. Expert Opinion on Therapeutic Patents, 2005, 15(2): 125−130.

[17] LI Xin, SHAN Guang-cun, ZHAO Hong-bin, SHEK C H. Domain knowledge aided machine learning method for properties prediction of soft magnetic metallic glasses [J]. Transactions of Nonferrous Metals Society of China, 2023, 33: 209−219.

[18] LOFFLER J F. Bulk metallic glasses [J]. Intermetallics, 2003, 11: 529−540.

[19] LIU Guang-qiao, KOU Sheng-zhong, LI Chun-yan, ZHAO Yan-chun, SUO Hong-Li. Effect of minor Fe addition on glass forming ability and mechanical properties of $Zr_{55}Al_{10}Ni_5Cu_{30}$ bulk metallic glass [J]. Transactions of Nonferrous Metals Society of China, 2012, 22(3): 590−595.

[20] LUKAS H. Computational thermodynamics [M]. Cambridge: Cambridge University Press, 2007.

[21] ZHANG Zhang, ZHANG Qi, JIN Li-ling, ZHANG Yin-ju, CAI Tian-yan, ZHAO Ling-yu, WANG Jian, JIN Zhao-yang, SHENG Li-yuan. Experimental determination of the phase equilibrium in the Mg–Cu–Ca ternary system at 350 °C [J]. Journal of Alloys and Compounds, 2020, 818: 25−51.

[22] WANG Jian, ZHANG Zhang, LI Shu, MENG Ling-zhong, CAO Zhan-ming, RAO Wei-feng. Experimental investigation and thermodynamic modeling of the Mg−Cu−Ca ternary system [J]. Calphad, 2021, 75: 105−116.

[23] LIU Bao-sheng, CAO Miao-miao, ZHANG Yue-zhong, HU Yong, GONG Chang-wei, HOU Li-feng, WEI Ying-hui. Microstructure, anticorrosion, biocompatibility and antibacterial activities of extruded Mg−Zn−Mn strengthened with Ca [J]. Transactions of Nonferrous Metals Society of China, 2021, 31: 358−370.

[24] WANG Jian, MENG Ling-zhong, JI Chen, WANG Rong-hua, ZHANG Ping-hu, JIN Li-ling, SHENG Li-yuan, ZHENG Yu-feng. Corrosion and in vitro cytocompatibility investigation on the designed Mg−Zn−Ag metallic glasses for biomedical application [J]. Journal of Magnesium and Alloys, 2024, 12(4): 1566−1580.

[25] ZHAO Ling-yu, XIN Yun-chang, JIN Zhao-yang, WANG Jian, FENG Bo, LIU Qing. Thermal stability of different texture components in extruded Mg−3Al−1Zn alloy [J]. Journal of Magnesium and Alloys, 2019, 7(4): 577−583.

[26] WANG Jian, HAN Jia-jia, DU Bei-ning, HUANG Yi-xiong, SHENG Li-yuan, RAO Wei-feng, WANG Cui-ping, LIU Xing-jun. Experimental and thermodynamic study of the Mg−Sn−Ca−Sr quaternary system: Part I — Mg−Sn−Ca ternary system [J]. Calphad, 2017, 58: 6−16.

[27] WANG Jian, ZHANG Zhang, ZHANG Yi-nan, HAN Dong, JIN Li-ling, SHENG L Y, CHANTRAND P, MEDRAJ M. Investigation on metallic glass formation in Mg−Zn−Sr ternary system combined with the CALPHAD method [J]. Materials Letters, 2019, 256: 126628−126631.

[28] BALE C W, BÉLISLE E, CHARTRAND P, DECTEROV S A, ERIKSSON G, GHERIBI A E, HACK K, JUNG I H, KANG Y B, MELANÇON J, PELTON A D, PETERSEN S, ROBELIN C, SANGSTER J, SPENCER P, van ENDE M A. FactSage thermochemical software and databases, 2010—2016 [J]. Calphad, 2016, 54: 35−53.

[29] GHOSH P, MEZBAHUL-ISLAM M, MEDRAJ M. Critical assessment and thermodynamic modeling of Mg−Zn, Mg−Sn, Sn−Zn and Mg−Sn−Zn systems [J]. Calphad, 2012, 36: 28−43.

[30] WANG Jian, HUDON P, KEVORKOV D, CHARTRAND P, JUNG I H, MEDRAJ M. Thermodynamic and experimental study of the Mg−Sn−Ag−In quaternary system [J]. Journal of Phase Equilibria and Diffusion, 2014, 35(3): 284−313.

[31] WANG Jian, CHARTRAND P, JUNG I H. Thermodynamic description of the Ag−(Ca, Li, Zn) and Ca−(In, Li) binary systems [J]. Calphad, 2015, 50: 68−81.

[32] HILLERT M, KJELLQVIST L, MAO H, SELLEBY M, SUNDMAN B. Parameters in the compound energy formalism for ionic systems [J]. Calphad, 2009, 33(1): 227−232.

[33] PELTON A D. A general “geometric” thermodynamic model for multicomponent solutions [J]. Calphad, 2001, 25: 319−328.

[34] WANG Jian, ZHANG Yi-nan, HUDON P, JUNG I H, MEDRAJ M, CHARTRAND P. Experimental study of the phase equilibria in the Mg–Zn–Ag ternary system at 300 °C [J]. Journal of Alloys and Compounds, 2015, 639: 593−601.

[35] KISSINGER H E. Reaction kinetics in differential thermal analysis [J]. Analytical Chemistry, 1957, 29: 1702−1706.

[36] ERINC M, SILLEKENS W H, MANNENS R G T M, WERKHOVEN R J. Applicability of existing magnesium alloys as biomedical implant materials [J]. Magnesium Technology, 2009, 5: 209−214.

[37] JIA Xue-jiao, SONG Jiang-feng, QU Xiao-rong, CAO Fu-yong, JIANG Bin, ATRENS A, PAN Fu-sheng. Effect of scratch on corrosion resistance of calcium phosphate conversion coated AZ80 magnesium alloy [J]. Transactions of Nonferrous Metals Society of China, 2022, 31(1): 147−161.

[38] HONG D, SAHA P, CHOU D T, LEE B, COLLINS B E, TAN Zong-qing, DONG Zhong-yun, KUMTA P N. In vitro degradation and cytotoxicity response of Mg−4%Zn−0.5%Zr (ZK40) alloy as a potential biodegradable material [J]. Acta Biomaterialia, 2013, 9(10): 8534−8547.

[39] WANG Xue-jian, CHEN Zong-ning, ZHANG Yu-bo, GUO En-yu, KANG Hui-jun, HAN Pei, WANG Tong-min. Influence of microstructural characteristics on corrosion behavior of Mg−5Sn−3In alloy in Hank’s solution [J]. Transactions of Nonferrous Metals Society of China, 2021, 31(10): 2999−3011.

可生物降解镁锌银非晶的设计与表征

王 见[1,2]，王 晨[1]，饶伟峰[3]，In-ho JUNG[2]

1. 扬州大学 机械工程学院，扬州 225009；
2. Department of Materials Science and Engineering, Seoul National University, Seoul 08826, Korea;
3. 齐鲁工业大学 机械与汽车工程学院，济南 250353

摘 要：为了开发用于生物可降解植入物的镁锌银非晶，采用相图计算(CALPHAD)和实验测量相结合的方法研究镁锌银合金的非晶成形能力(GFA)和生物相容性。对 $Mg_{96-x}Zn_xAg_4$ 和 $Mg_{94-x}Zn_xAg_6$ (x=17，20，20，23，26，29，32，35)两种合金系列的高 GFA 潜力进行理论预测，并通过实验测试进行证实。采用 X 射线衍射(XRD)和差示扫描量热法(DSC)评价这些合金的结晶度、GFA 值和结晶特性。根据目前的结果，成分介于 $Mg_{73}Zn_{23}Ag_4$ 和 $Mg_{64}Zn_{32}Ag_4$ 之间的 $Mg_{96-x}Zn_xAg_4$ 系列合金以及成分介于 $Mg_{66}Zn_{28}Ag_6$ 和 $Mg_{63}Zn_{31}Ag_6$ 的 $Mg_{94-x}Zn_xAg_6$ 系列合金具有良好的 GFA。值得注意的是，$Mg_{96-x}Zn_xAg_4$ 系列的 GFA 优于 $Mg_{94-x}Zn_xAg_6$ 系列。此外，合金 $Mg_{70}Zn_{26}Ag_4$、$Mg_{74}Zn_{20}Ag_6$ 和 $Mg_{71}Zn_{23}Ag_6$ 具有可接受的腐蚀速率和细胞相容性，对细胞增殖有积极作用。这些特性使它们适合应用于医疗环境中，有可能作为可生物降解植入物的材料。

关键词：非晶成形能力；相图计算；镁锌银非晶；细胞相容性

(Edited by Xiang-qun LI)